



HAL
open science

Microstructural damage behaviour of Al foams

Jutta Luksch, Thomas Bleistein, Kristian Koenig, Jérôme Adrien, Éric Maire,
Anne Jung

► **To cite this version:**

Jutta Luksch, Thomas Bleistein, Kristian Koenig, Jérôme Adrien, Éric Maire, et al.. Microstructural damage behaviour of Al foams. ACTA MATERIALIA, 2021, 208, 10.1016/j.actamat.2021.116739 . hal-03483003

HAL Id: hal-03483003

<https://hal.science/hal-03483003v1>

Submitted on 7 Mar 2022

HAL is a multi-disciplinary open access archive for the deposit and dissemination of scientific research documents, whether they are published or not. The documents may come from teaching and research institutions in France or abroad, or from public or private research centers.

L'archive ouverte pluridisciplinaire **HAL**, est destinée au dépôt et à la diffusion de documents scientifiques de niveau recherche, publiés ou non, émanant des établissements d'enseignement et de recherche français ou étrangers, des laboratoires publics ou privés.

Microstructural damage behaviour of *Al* foams

Jutta Luksch¹, Thomas Bleistein¹, Kristian Koenig¹, Jérôme Adrien², Eric Maire² and Anne Jung¹

¹ Saarland University, Applied Mechanics, Campus A4.2, D-66123 Saarbruecken, Germany

² Université de Lyon, Laboratory MATEIS - INSA Lyon, F-69621 Villeurbanne, France

Abstract

Metal foams are cellular materials, which can be manufactured with different cellular structures, such as open- or close-cell foams. In addition, the manufacturing conditions influence the microstructure and thus the mechanical properties of the foam. Its global mechanical behaviour is related to its local mechanical behaviour, which means the strut and its microstructure, results in the so-called structure-property relationship [1].

Motivated by a large variation of the tensile properties in earlier studies of open-cell aluminium foams [1] the correlation between the microstructure and the mechanical behaviour in tensile experiments is investigated in this study. Tensile experiments on individual struts are conducted both *in situ* and *ex situ*. *In situ* experiments yield more details and are complemented by *ex situ* experiments, which are easier to perform, thus provide better statistics.

Tensile experiments on individual aluminium struts are executed *in situ* applying X-ray computed tomography. This information is used to analyse the microstructural failure mechanisms. The focus of the investigation is on the failure analysis at crack initiation and crack propagation.

Additionally, *ex situ* tensile experiments of individual struts are performed. To correlate the microstructure with their mechanical properties the struts are characterised with micro X-ray computed tomography in advance. Furthermore, the microstructure is analysed via optical microscopy, scanning electron microscopy and energy dispersive X-ray diffraction.

Keywords: micro X-ray computed tomography, in situ micro tensile test, open-cell aluminium foam, microstructure

1. Introduction

Cellular materials have great potential as lightweight materials and for crash absorption, e.g. in cars [2, 3, 4, 5]. It is therefore desirable to establish them as a multifunctional material in industry [6]. The structure of trabecular bones, wood, coral or cork are examples for cellular materials in nature [2, 7]. Inspired by nature, there are man-made materials such as foams, honeycombs and auxetics [8].

Cellular materials are microheterogeneous materials, which means the material properties are a superposition of structural effects and the properties of the base material. To describe such materials, it is helpful to consider them on different length scales, using the hierarchical concept [9, 10, 11]. In this concept different feature structures are characteristic for each length scale. Typically, it goes from macro via meso to micro scale.

The open-cell aluminium (*Al*) foam investigated can be described using this hierarchical concept: the micro scale covers the microstructure of the material and the smallest geometric unit, the foam struts. The next bigger geometric unit comprises a few single pores, consisting of struts connected by nodes, belonging to the meso scale. The macro scale is defined by a representative number of pores, such that the properties are independent of the sample size. Hence, it comprises, small samples up to the entire component made of foam. The microstructure can be characterised by grain size, precipitates, pores and the chemical composition of the alloy. Pores are further characterised via their shape, size and orientation [12, 13].

From the multi scale nature of metallic foams it becomes clear that the parameter space is large including not only the microstructure of the alloy and the design of the component but also size, shape and orientation of struts, nodes and pores. This makes an empirical approach to tailor mechanical properties inefficient and expensive. Therefore, establishing a structure-property relationship is a critical task to accelerate the development of metallic foams for industrial applications [1, 14].

The *Al* foam analysed in this work is manufactured by investment casting with the casting alloy $AlSi_7Mg_{0.3}$. Due to the manufacturing conditions the cooling velocity is significantly faster than for the production of bulk material. The properties of the strut material cannot be assumed to be equal to the material properties from bulk material [1, 15, 16]. Additionally, the

surface-to-volume ratio is different and surface inhomogeneities play an important role for foams. All these points make it crucial to analyse individual foam struts.

Mechanical testing of the individual foam struts is challenging due to their individual shape and small size of a few millimetres in length and less than one millimetre in width. This size is between the size of a standard macroscopic test rig and a standard *in situ* micro testing rig. Custom-built rigs adapted to single struts and individual clamping of the struts are the solution to this challenge [1, 17, 18]. Due to the individual shape, rough surface and inhomogeneities of the struts, a lot of experiments are needed to get a robust result. One single experiment of a strut takes approximately 2-3 hours from the extraction of the strut out of the foam to the evaluation of the stress-strain data.

Jung et al. [1] observed an important variation in the mechanical properties of single struts. *Al* foam struts and nickel aluminium-(*Ni/Al*)-hybrid foam struts were investigated under tension *in situ* using scanning electron microscope (SEM) and *ex situ* to obtain statistical results. Stress-strain diagrams were created and showed a large scattering. Additionally, the deformation mechanism of single struts and foam pores was observed *in situ* in SEM.

To explain the variation of the results from Jung et al. [1] the analysis of Mukherjee et al. [13] is interesting. They found pores in the cell walls of a closed-cell *Al* foam, produced by a powder metallurgical route. It is known that the casting route also causes porosity which leads to damage and failure. A combination of micro X-ray computed tomography (μ CT) with mechanical testing enables to relate the porosity with, for example the fracture strength [19, 20]. This porosity depends on the manufacturing conditions, but up to now, there was no analysis correlating the microporosity and the mechanical properties of the foam. Profound knowledge of the structure-property relationship is necessary to tailor the mechanical properties by the manufacturing process.

Fischer et al. [21] analysed the influence of the mould and casting temperature of an *Al* (A356) open-cell foam on the microstructure and the macroscopic compression behaviour. They found, that the influence of the moulding and casting temperature depends on the strut diameter of the foam. The influence is bigger on smaller foam struts and it is different than in bulk material.

Amani et al. [22] carried out a study analysing the microstructure and its effect on the mechanical properties. The results were compared with finite

element (FE) simulations based on μ CT scans of an open-cell 6101 Al foam. They found a strong geometrical impact of the inhomogeneous foam struts and an impact of the distribution of intermetallic particles.

The present work investigates the reason for the scatter and variation of the mechanical properties of individual struts. Manufacturing by investment casting leads to a coarse surface of the struts. In addition, the *Al* casting alloy forms precipitates and shrinkage can induce pores in the strut. For the analysis of the microstructure and correlation of the mechanical properties of single struts a non-destructive examination method, X-ray computed tomography, and an investigation procedure for measuring the mechanical properties by tensile tests on individual struts are applied.

2. Materials and methods

2.1. Aluminium foams and microstructural characterisation

Al foams with a pore size of 20 ppi were produced by Celltec Materials GmbH (Dresden, Germany) using investment casting with the casting alloy $AlSi_7Mg_{0.3}$. Alloys in the group $AlSiMg$ have good casting properties and are corrosion resistant. Table 1 shows the chemical composition of the alloy.

Table 1: Chemical composition of the *Al* casting alloy $AlSi_7Mg_{0.3}$ with the elements: magnesium (*Mg*), silicon (*Si*), titanium (*Ti*), iron (*Fe*), manganese (*Mn*), zinc (*Zn*) and copper (*Cu*) (data from personal communication with Celltec Materials GmbH).

Element	<i>Mg</i> /%	<i>Si</i> /%	<i>Ti</i> /%	<i>Fe</i> /%	<i>Mn</i> /%	<i>Zn</i> /%	<i>Cu</i> /%
Max	0.45	7.5	0.18	0.15	0.10	0.07	0.03
Min	0.30	6.5	0.10	-	-	-	-

The main alloy elements are *Zn*, *Cu*, *Mn*, *Mg* and *Si*, which improve the strength of the alloy. The secondary element *Fe* has a low solubility in *Al* and forms intermetallic phases. As a result, *Fe* has a strong influence on the fracture properties of *Al* alloys. The shape of the *Fe* intermetallic phases depends mainly on the *Mg* fraction. Pores or small holes result from shrinkage during cooling [13, 23, 24].

In order to characterise the microstructure of the *Al* foam one strut is embedded with conductive, low melting Wood’s alloy for further preparation. The following step is grinding with 800, 1200 and 2500 grids and polishing

with 6 μm , 3 μm and 1 μm diamond suspension from ATM GmbH (Mammelzen, Germany). The final 15-minutes polishing is performed with a colloidal *Si* suspension, OP-U NonDry from Struers (Willich, Germany). Following the preparation the cross section is analysed in an SEM and by energy dispersive X-ray (EDX) diffraction using a Sigma SEM from Carl Zeiss AG (Oberkochen, Germany) and an EDX system X-Max 20 mm² from Oxford Instruments (Abingdon, UK).

2.2. *In situ* tensile tests

μCT is a non-destructive investigation method to obtain 3D information of a material [25, 26]. For laboratory high resolution devices an X-ray source with a small focus and a detector with high resolution is necessary. Larger distances between sample and detector increase the magnification. The absorption contrast of a μCT scan is based on the difference in the atomic number of the elements. This means that the contrast between *Al* and *Fe/Ti* is easily visible in a μCT scan, whereas *Si* and *Mg* do not cause high contrast. As a consequence, only precipitates with *Fe* or *Ti* and pores due to shrinkage can be detected.

Figure 1 shows the custom-built test rig that was used to perform *in situ* μCT tensile tests. These experiments were conducted with a high resolution laboratory tomograph EasyTom nano designed by RX Solutions (Chavanod, France) at MATEIS laboratory at the Institut National des Sciences Appliquées de Lyon. In the following, the data recorded with this device is referred to as HR μCT data. The upper fixture of the test rig is connected with a carbon fibre tube to support the load while limiting the attenuation of the X-rays in order to obtain good quality scans from the sample. The lower fixture moves downwards to achieve a tensile load on the moulded sample between the upper and lower fixture.

For the tensile tests struts are carefully extracted using a small side cutter to avoid pre-damaging [1, 27]. A single strut with the nodes on both ends remains. Wood's alloy is used for moulding because of easy processing due to the low melting temperature of about 71 °C, which does not have any influence on the mechanical properties of the *Al* strut. The strut has to be aligned carefully such that its axis is parallel to the tensile axis in order to achieve uniaxial stress conditions. The experiment is performed stepwise with a HR μCT scan conducted after every loading step. The force and displacement data are collected and correlated with the HR μCT scans.

X-ray tomography experiments were performed at high resolution using the

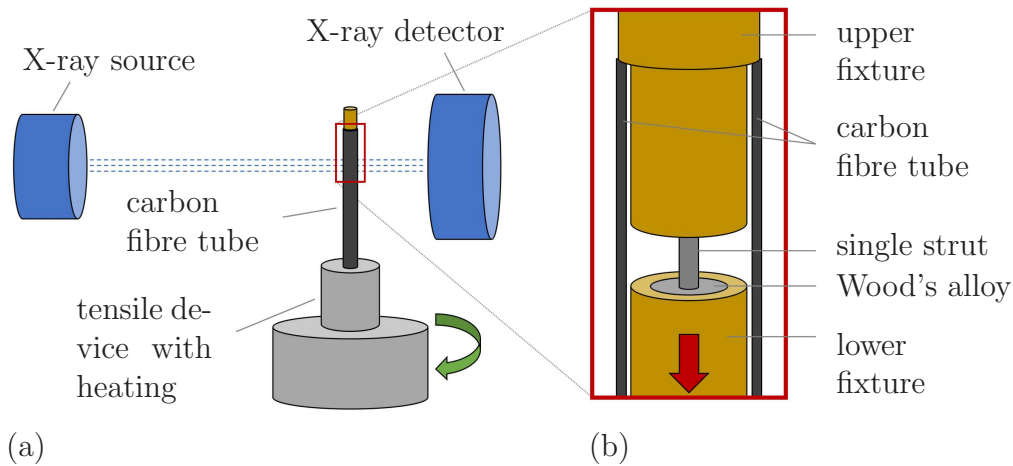


Figure 1: (a) Schematic drawing of the *in situ* tensile test setup with the custom-built tensile device in the HR μ CT device with the X-ray source and detector, (b) magnification of the fixture of the single strut into the carbon fibre tube.

laboratory tomograph. The Hamamatsu X-ray source was operated with a LaB_6 cathode at a voltage of 100 kV. The detector was a Hamamatsu CCD camera with a pixel size of $12 \mu\text{m}$. The Al struts were scanned at a voxel size of $0.7 \mu\text{m}$. Each scan consisted in 1600 projections recorded with a continuous rotation around 360° with an exposure time of 3 s for each. The total acquisition time was 1 h 30 minutes. The cone-beam XCT data were reconstructed by a filtered back projection Feldkamp-algorithm.

2.3. *Ex situ* tensile tests

After carefully extracting a high number of single struts a fast lower resolution, following LR μ CT scan with a resolution between $3 \mu\text{m}$ and $4 \mu\text{m}$ is performed in order to capture the microstructure of the strut before *ex situ* testing. This is achieved using another, lower resolution but very fast tomograph, the *phoenix v|tome|x s* Industrial High-Resolution CT & X-ray System from *BakerHughes, a GE Company* (Houston, USA) at MATEIS laboratory. The X-ray source was operated at a voltage of 80 kV. Each scan consisted in 360 projections recorded with a continuous rotation with an exposure time of 0.333 s for each. The total acquisition time was 2 minutes. After this initial LR μ CT scan, the samples were tested in tension, outside of the tomograph. The custom-built microtesting device and clamping method are the same as used by Jung et al. [27], which was built to analyse small

samples such as individual foam struts or fibres within a reasonable time and low costs. The top of the sample is fixed in a stationary clamping, while the bottom of the sample is moved downwards with a motor. For clamping the individual foam struts get moulded into Wood's alloy in the spelter socket of the testing device. The force is measured by an exchangeable S-type load cell. The device is controlled by an in-house LabVIEW[®], National Instruments (Austin, USA), program.

Wood's alloy is used for moulding the strut samples in the *ex situ* microtesting device. The final moulding step has to take place inside the device, since thermal expansion of the Wood's alloy while cooling can exert a load on the sample. To prevent such a pre-loading, the displacement is adjusted such that the force on the sample does not exceed ± 0.3 N. The experiment is started half an hour after the moulding to guarantee that the strut has cooled down to room temperature. The experiments are performed in a displacement-controlled mode with a machine speed of 0.02 mm/s. For crack observation, pictures are taken every 0.005 mm with a CCD-camera, Manta 235B from Allied Vision (Stadtroda, Germany) with a telecentric lens, TC23016 from Opto Engineering (Mantova, Italy). The force and displacement data are collected for further analyses. When the force drops to zero the strut has failed and the experiment is finished.

After the experiment, the broken sample is characterised. The position of the crack location is measured and the fracture faces are analysed via SEM. An evaluation of the initial LR μ CT data is conducted. The cross sectional area is taken from the initial 3D reconstruction of the LR μ CT data at crack position. Pores are identified with a global threshold by segmentation with the open source software Fiji, ImageJ [28]. For later comparison of the samples the maximal engineering stress is calculated.

3. Results and discussion

3.1. Evaluation of the LR μ CT data regarding the strut geometry

The LR μ CT data of all 16 *ex situ* tested struts enable a statistical comparison of the strut geometry. When extracting the struts, only long and straight struts were selected for proper results in tensile tests. The following results can only be applied to this pre-selected group. Figure 2 illustrates the definition of the strut geometry parameters. The smallest cross sectional area A_{\min} of each strut is taken for comparison. After careful literature research no definition of strut length, where it is defined without nodes, was found.

Jung et al. [14] studied foam parameters, but included the nodes into the strut length. We thus arbitrarily made the decision that the ends of the strut length are defined as the points where its cross sectional area is two times A_{\min} (Fig. 2 marked red), since this outlines a tremendous increase in local strut thickness, which can only be found in the vicinity of the nodes. The strut length determined in this way lays in the region of the length measured by Jung et al. [14] for the same foam. Hence, such a definition based on the smallest cross sectional area is reasonable. To compare the porosity of the struts, the pore volume fraction is determined by taking the ratio of the pore volume and the total volume into account.

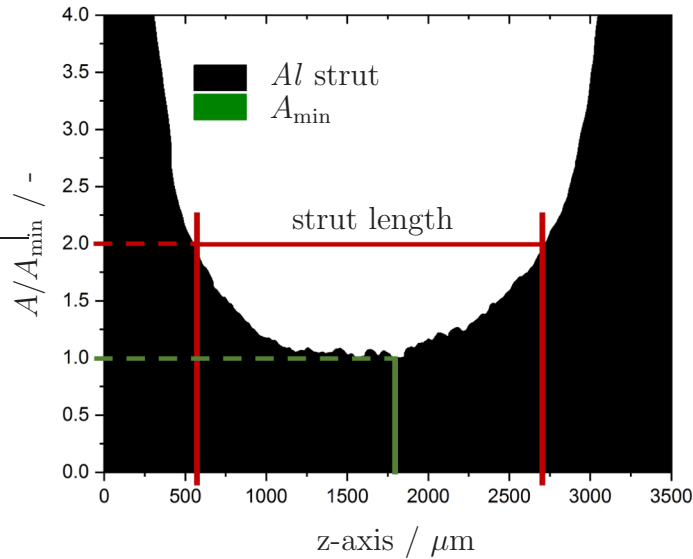


Figure 2: Exemplary plot of normalised strut cross sectional area A/A_{\min} versus length.

Figure 3 shows the measured value of porosity (a) and A_{\min} (b) as a function of the strut length. The distributions outline a wide range of the characteristic values which underlines the irregular shape and inhomogeneities in the foam struts (see Fig. 3). The pore volume fraction and A_{\min} show no correlation with the strut length.

3.2. Investigation of the microstructure by LR μCT , optical microscopy, SEM and EDX

To obtain the full information about the microstructure one strut was investigated both by LR μCT scanning and by a metallographic preparation

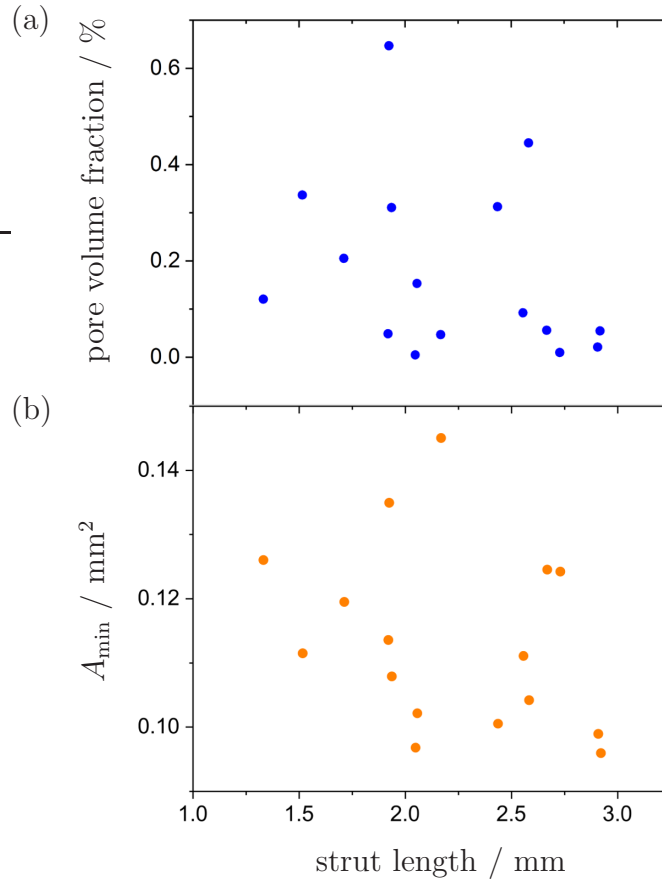


Figure 3: (a) Pore volume fraction and (b) minimum cross sectional area A_{\min} as a function of the strut length.

for the analysis of the precipitates and primary inclusions via SEM and EDX. Figure 4 (a) - (i) shows images from LR μ CT, optical microscopy and SEM as well as EDX analyses conducted from the same position for comparison. The contrast in the LR μ CT scan outlines just one precipitate while the images of optical microscopy and SEM show more precipitates with different brightness and contrasts. The shapes of the various types of precipitates are different. The shape of Fe primary inclusions depends on the amount of Mg [23]. This is clearly visible in Figure 4 (f) and (g). The primary inclusion in the middle is without Mg and the one on the lower left is with Mg and has a much finer shape. The atomic numbers of Si and Mg are only one or two numbers away from Al , so that the contrast in the LR μ CT images is

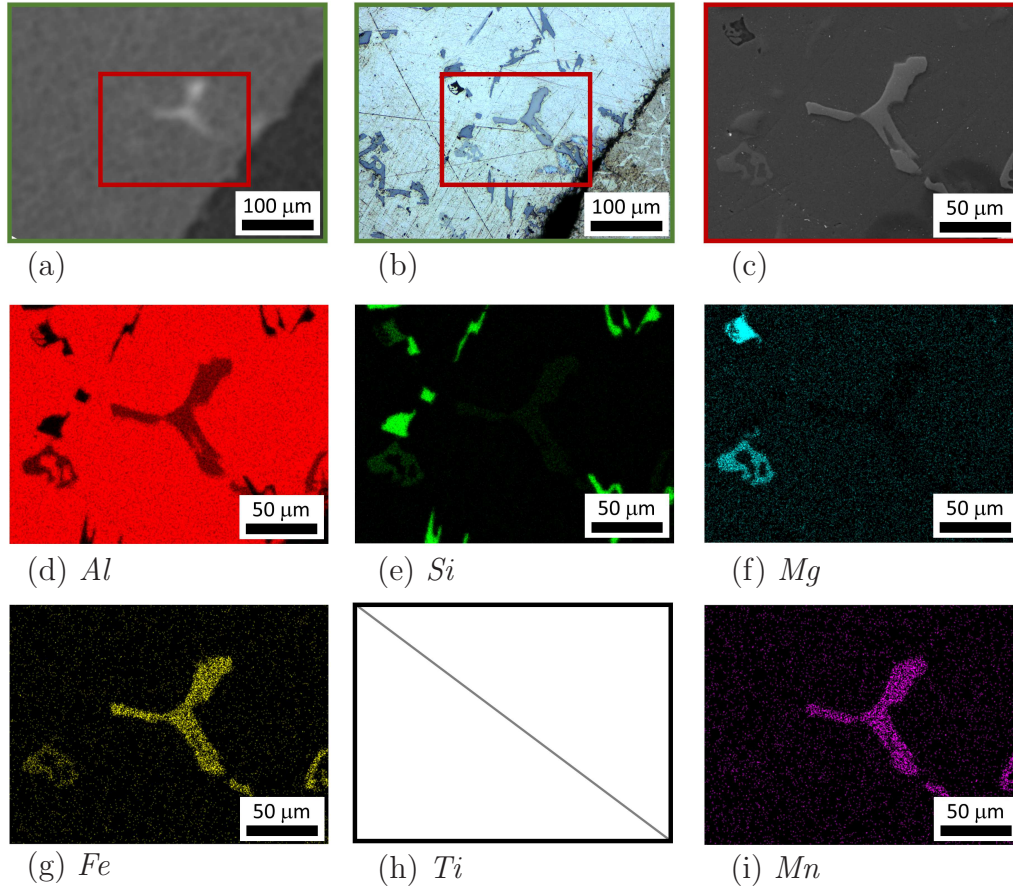


Figure 4: (a) LR μ CT image, (b) optical microscopy image, (c) - (i) magnified sections of (a)/(b), (c) SEM image and (d) - (i) EDX element mapping of the sample position with the corresponding element indicated below the image.

below the detection limit. Therefore, the EDX mapping validates that only *Fe* and *Mn* precipitates and primary inclusions are visible in the LR μ CT images. No *Ti* was detected at this position. Due to the small size of the analysed position compared to the total foam size, the composition is not representative for the average.

3.3. *In situ* HR μ CT tensile tests

With the stepwise *in situ* HR μ CT tensile tests the microstructure can be observed during testing from the beginning of fracture up to failure of the strut. Figure 5 shows a force-displacement curve and the respective re-

construction of the *Al* strut at different loading steps with their corresponding microstructure. The first, unloaded reconstruction of the sample (see Fig. 5 (b)), shows one small pore and few evenly distributed primary inclusions. In the second and third reconstruction (see Fig. 5 (c), (d)) a stretching and reduction of the cross section is visible but no new damage can be detected. The crack, which leads to failure of the *Al* strut occurs only in the last step (see Fig. 5 (e)). The cross sectional area in the crack location before the test was 0.140625 mm^2 resulting in a maximal engineering stress of 120.18 MPa.

Figures 6 and 7 show respectively two struts with little pre-cracks in their initial state, which were chosen to understand the microstructural failure process. The pre-cracks can result from manufacturing and also possible be induced by the cuttings. While the force-displacement curve is not meaningful due to these pre-cracks, the interaction of cracks with primary inclusions can be highlighted. In Figure 6 (c) the strut is shown only with the main crack and the primary inclusions in that area. Two details are zoomed in the orange and green box for better understanding. In the orange box a big primary inclusion cuts by few small cracks and in the green box a big crack divides one primary inclusion such that the primary inclusion lays on the crack flanks.

Figure 7 (a)-(d) shows a sequence of HR μ CT images. The initial step shows the primary inclusions and pores without any load, and the last image shows the failed strut and a crack along a primary inclusion. The intermediate steps illustrate the formation of the crack within the area of small pores along a primary inclusion. These observations underline the hypothesis that inhomogeneities like primary inclusions and pores are the starting points of microcracks. The microcracks then get bigger and join to form cracks and in the end a fracture, which leads to the failure of the strut. A similar kind of failure mechanism with first the occurrence of microcracks in the primary inclusions and after that a coalescence of them to the failure was found by Wang [29] in bulk *Al* casting alloy.

To conclude, there are two mechanisms of failure. One mechanism, shown in Figure 6 (c) is small cracks in a big spherical primary inclusion. The second mechanism, Figure 6 (c) and 7 (d), is the occurrence of a big crack through a primary inclusion with *Fe*-rich inclusions on the crack flanks.

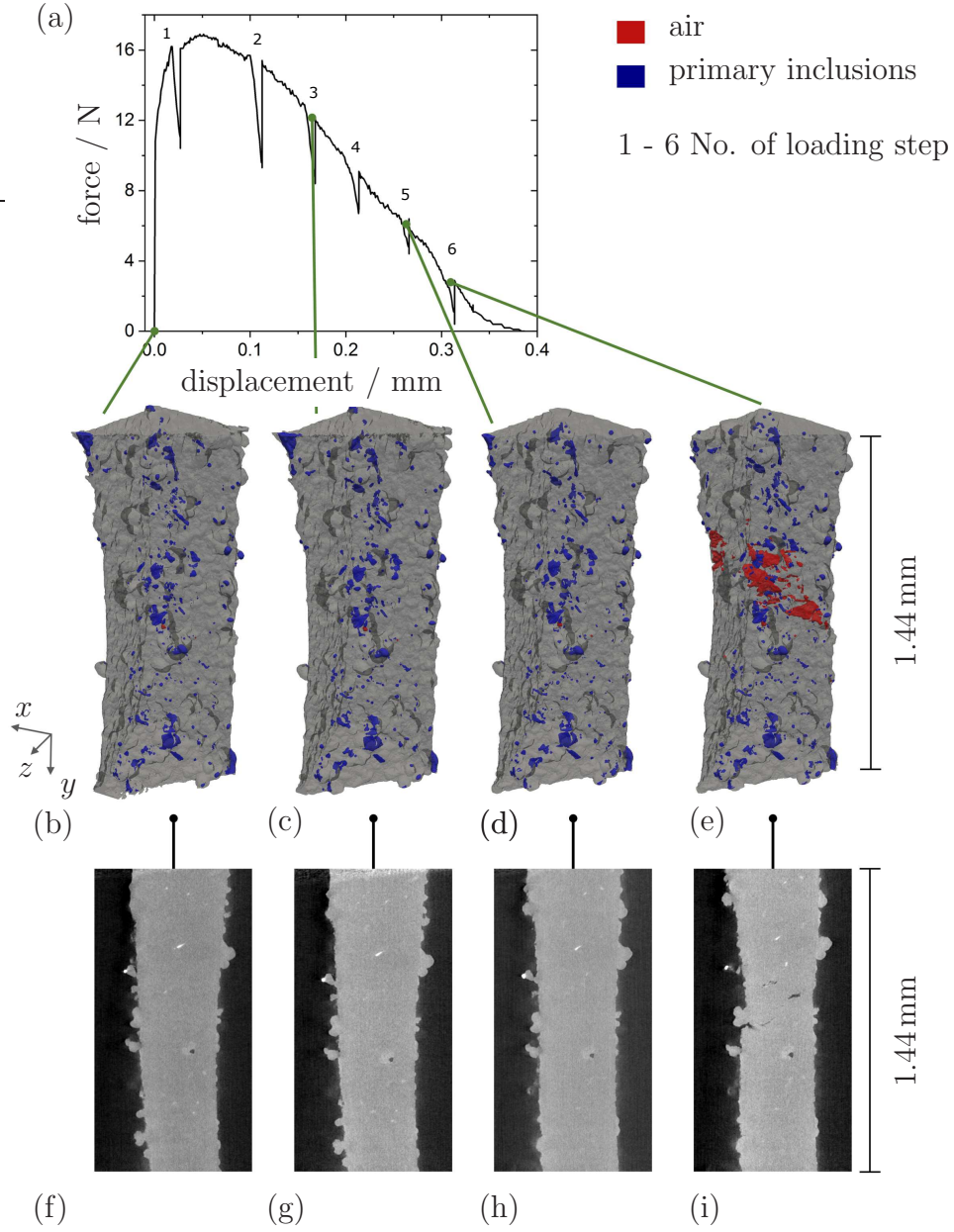


Figure 5: (a) Force-displacement curve of an *in situ* tensile test, (b) Al strut before tensile test, (c) Al strut at the third loading step, (d) Al strut at the fifth loading step and (e) Al strut after failure of the strut. (f) - (i) corresponding HR μ CT slices of the steps.

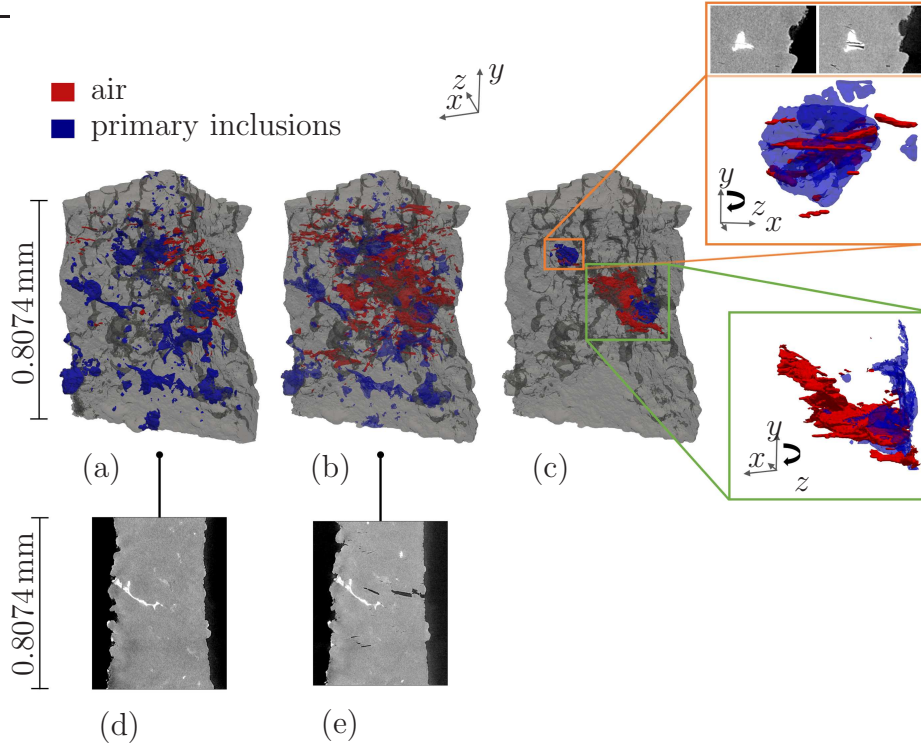


Figure 6: (a) *Al* strut before tensile test with little pre-cracks (red), (b) *Al* strut after tensile test, (c) *Al* strut after tensile test with only the main crack and the corresponding primary inclusion in color, orange detail: spherical primary inclusion with cracks inside and the corresponding HR μ CT slices; green detail: main crack with the corresponding primary inclusion on the crack surfaces. (d) - (e) HR μ CT slices of the initial and the last state of tensile test.

3.4. *Ex situ* LR μ CT tensile tests

3.4.1. Classification of the struts into categories

Due to a non-uniform distribution of pores, the struts are classified according to the size and location of the pores. Category 1 contains samples without pores. Samples with pores in the nodes only are category 2 and samples with pores in the struts only are category 3. In category 4, there are samples with pores in both the nodes and the strut. A summary of the categories with examples is shown in Figure 8. From a set of pre-characterised samples, five of each category are selected. For category 3 however the set contains only one sample.

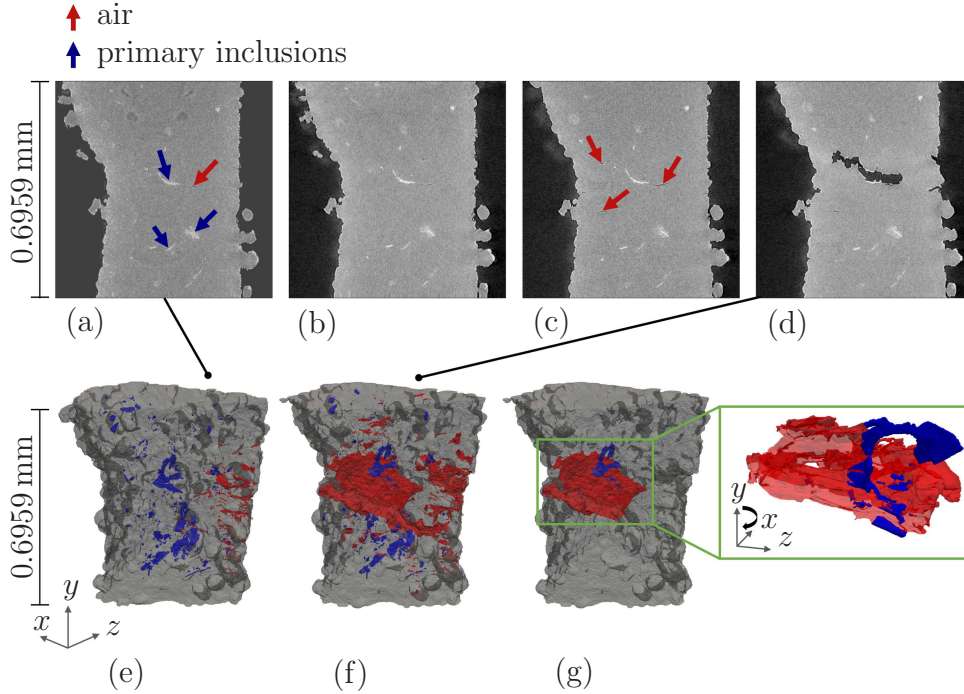


Figure 7: HR μ CT images and corresponding 3D reconstruction of one strut at different times during an in situ tensile test. (a) - (d) HR μ CT slices of different states with arising cracks, (e) 3D reconstruction before tensile test with little pre-cracks on the right, (f) 3D reconstruction after tensile test, (g) 3D reconstruction after tensile test with only the main crack and the corresponding primary inclusion, detailed view of the main crack with the corresponding primary inclusion on the crack surfaces.

3.4.2. Correlation between the mechanical properties and categories of the struts

Figure 9 illustrates the maximal engineering stress for each sample related to its category. For better comparison of the categories the mean of the maximal engineering stress over the categories is illustrated with a red triangle. The struts without pores have the highest maximal engineering stress average of all categories. Pores are then clearly shown here to be weak points in the microstructure of the struts and lead to lower maximal engineering stresses. For category 3 the statement is not strong due to its small amount of samples. The samples with pores all over the struts are widely spread in the maximum engineering stress. That means that the presence of pores does not necessarily lead to lower maximal engineering stress.

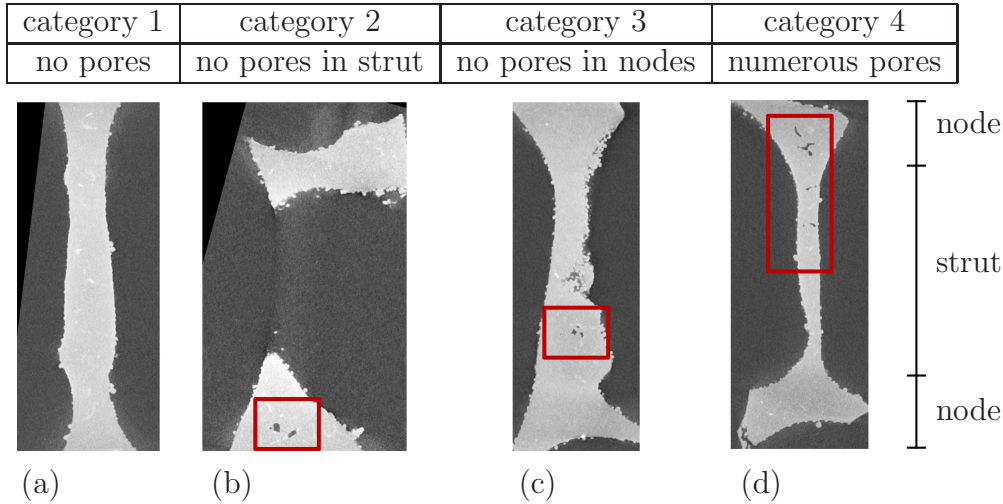


Figure 8: Classification of samples into categories by pore size and position, (a) category 1, (b) category 2, (c) category 3 and (d) category 4. The position of pores is indicated by red boxes.

In summary, pores in the samples lead to a bigger variation of the maximal engineering stress in tensile tests. To include the *in situ* tested struts, due to the presence of pre-cracks in two of the three *in situ* tested struts the maximal engineering stress was only determined for the one without pre-cracks, which had a maximum engineering stress of 120.18 MPa. Comparing the maximum engineering stress of the *ex situ* data this strut lays in the region of category 2 to 4. The nodes of the *in situ* strut are not characterised such that a classification is not possible. One could assume that the cracks and failures appear on the pores or primary inclusions in the struts. However, further analysis is necessary to determine whether this is true because in the analyses above no statement about crack position with respect to pore position was made.

3.4.3. Correlation between the mechanical properties and the microstructure in the crack location

To better understand the microstructure in the crack location, strut profiles of the LR μ CT data of each strut along its length axis were used. An example is shown in Figure 10(a). The normalised cross sectional area, referenced to A_{\min} , is plotted against the strut length.

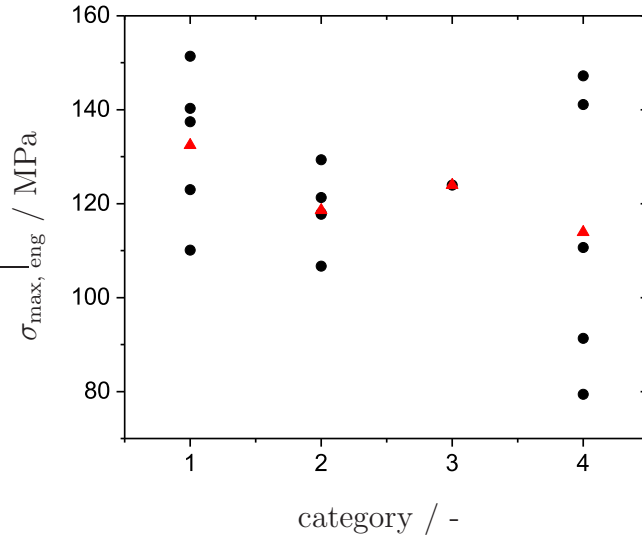


Figure 9: Maximal engineering stress $\sigma_{\max, \text{eng}}$ as a function of the categories, average of the maximal engineering stress of each category in red.

In Figure 10 the area corresponding to pores is indicated in blue, the section of the smallest cross sectional areas, defined by all smallest cross sections $N_{A_{\min 200\mu\text{m}}}$ resulting in a section of $200\mu\text{m}$ of the strut length, is shown in green and the crack location is marked in red. The crack location was located by the observation of the taken pictures during and after the test on each strut since the crack runs not perpendicular to the loading direction in order to observe the correlation between the crack location and the initial microstructure in that region. Since the crack location (Fig. 10 (b) red) covers not the entire part of smallest cross sectional areas $N_{A_{\min 200\mu\text{m}}}$ (Fig. 10 (b) green) for an objective comparability the fraction $A_{\%}$ of smallest cross sectional areas in the crack location $N_{A_{\min 200\mu\text{m}}\text{crack}}$ is calculated for each strut (Fig. 10 (b)). For a second characteristic the biggest pore cross sectional area in the crack location in each strut was measured (Fig. 10 (c)). For comparing the struts the two characteristics were plotted against the maximal engineering stress (Fig. 11).

The maximal engineering stress is plotted against the maximal pore size in the crack location of the struts in Figure 11 (a). A division of the group into two parts is evident from the figure. Struts in the first part have smaller pores and higher maximal engineering stress while struts in the second part have bigger pores of about 0.035 - 0.045% of the normalised area and lower

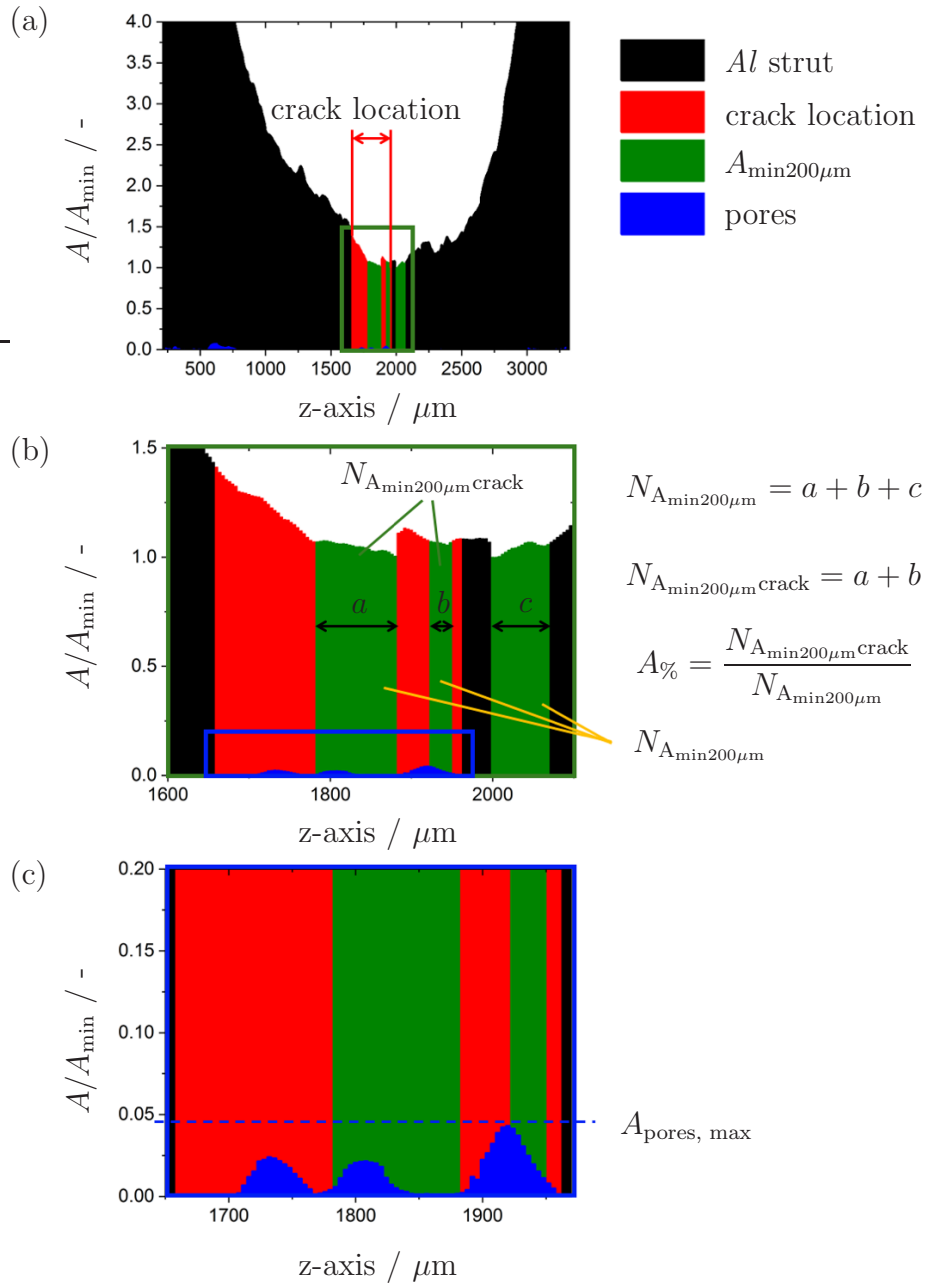


Figure 10: (a) Profile of a strut, (b) $A_{\%}$: fraction of smallest cross sections in the crack location and (c) maximum pore cross sectional area in the crack location $A_{\text{pores, max}}$.

sectional area in contrary to what could be expected. A large fraction $A\%$ of smallest cross sectional area in the crack location leads to slight increase in the maximal stress (Fig. 11 (b)). This could be explained that a pore which leads to a crack weakens struts also in areas far away from smallest cross sectional area. The maximal engineering stress is plotted against the fraction of the smallest cross sectional areas in the cracked location. Three samples have no smallest cross sectional area in the crack location and show low maximal engineering stress. The samples with a bigger fraction of smallest cross sectional areas in the crack location resist a higher engineering stress. Consequently, if failure occurs in samples where the smallest cross sectional areas $N_{A_{\min 200\mu m}}$ (Fig. 10 (b) green) is totally not in the crack location (Fig. 10 (b) red) the failure must be caused by other reasons such as pores or inclusions.

For a deeper analysis one of those samples will be fully examined here. Figure 12 (a) shows the profile of the strut with the smallest cross sectional area, crack location and pores marked. The fracture face of this sample was analysed by SEM as shown in Figure 12 (c). The corresponding LR μ CT image is shown in Figure 12 (b). The strut profile outlines that the smallest cross sections are not in the crack location. However, a big pore is in the crack location, which is visible in the SEM on the fracture surface of the strut. The corresponding LR μ CT image shows the same shape of the pores, which confirms the methodology used here. Jiang et al. [30] also found shrinkage pores on fracture surfaces of cast *Al* foam struts.

4. Conclusion

The present work investigates the correlation between the mechanical properties and the microstructure of *Al* foam struts. As in literature [1, 15] the bulk material from the same alloy has different mechanical properties than the strut material from the present *Al* foam due to different cooling velocity during manufacturing, micro stresses and large surface-to-volume ratio resulting in different microstructure. Due to the large surface-to-volume ratio defects (oxides, pores and intermetallics) have a stronger impact on the mechanical properties than in bulk material. The analysis of single struts is unavoidable. HR and LR μ CT data of single struts were collected and 3 *in situ* as well as 16 *ex situ* tensile tests were conducted.

The two different analysing routines are used to combine the benefits of *in situ* HR μ CT and *ex situ* microtensile tests. The *in situ* experiments re-

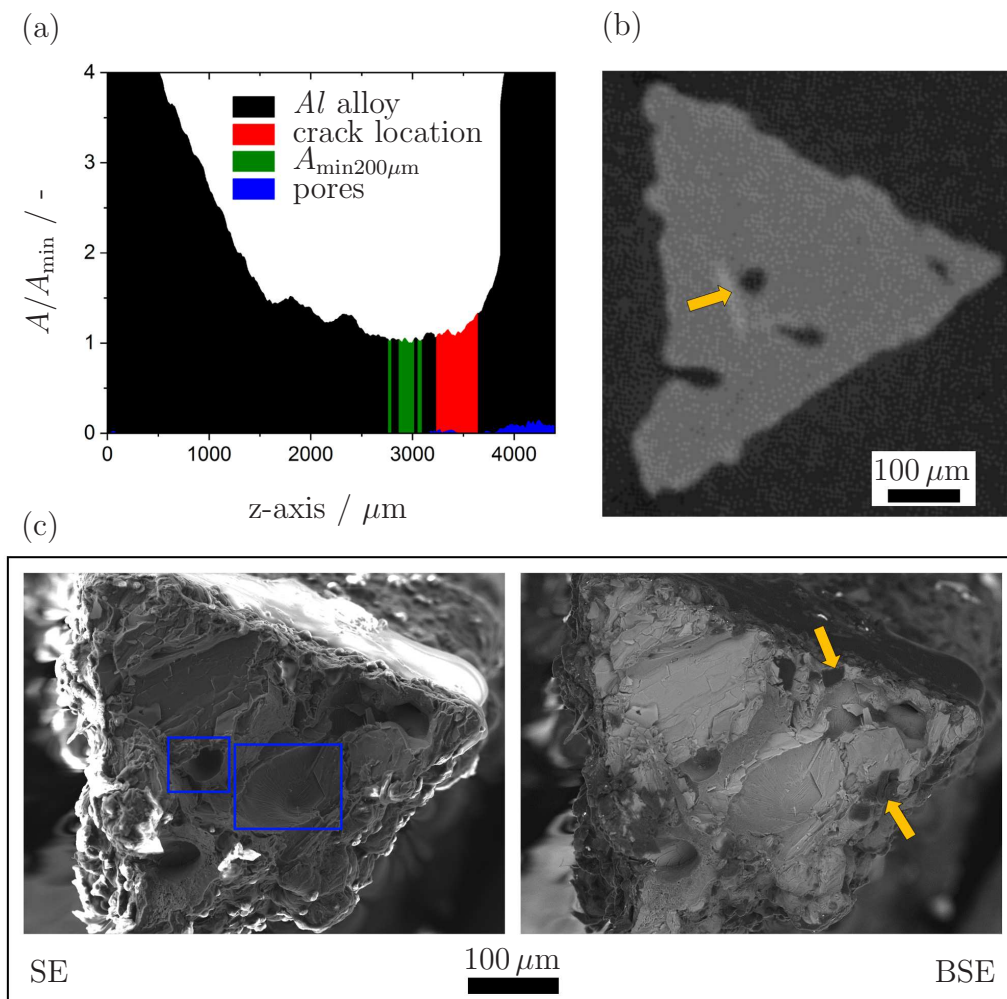


Figure 12: Examination of an exemplary strut (a) strut profile with the smallest cross section A_{\min} , crack location and pores marked, A_{\min} is not in the crack location, but pores are visible in the crack location (b) LR μCT image of the crack location with big pores and a primary inclusion (yellow arrow) (c) fracture surface from secondary electrons (SE) and back-scattered electrons (BSE) images of the same position, blue boxes mark pores of different characteristics.

veal the microstructure of the foam strut during the tensile test in different discrete time steps. Therefore, the damage development can be directly correlated to the loading steps. Disadvantages of this testing routine are the long measuring times and the increased complexity of the experiment in the tomograph. The *ex situ* tensile tests are performed on samples which

were pre-characterised using faster but lower resolution LR μ CT. A post-characterising routine is used to correlate the mechanical behaviour with the microstructure of the struts. The benefit of *in situ* tests is the understanding of the influence of the microstructure on the failure position in a strut and the benefit of *ex situ* tests is a short measuring time for statistic analysis.

The maximal engineering stress was measured and combined with the microstructure of the struts. From the LR μ CT data the geometry of struts was analysed and characterised by their minimum cross sectional area and length. Longer struts seem to have a smaller cross sectional area, but more data is required for a conclusive statement on this aspect.

The *in situ* tensile tests show two different crack propagations in primary inclusions. First, parallel microcracks appear in a big primary inclusion and secondly primary inclusions are divided by a crack. This statement can only be applied to the primary inclusions, which are composed of *Fe/Ti* because those composed of *Mg/Si* are not visible in the HR μ CT contrast. The struts were categorised by their global microstructure for *ex situ* tensile testing. While some correlation between the categories and the maximal engineering stress was visible, more data is needed to confirm. Overall, the global microstructure seems not to play a big role in the maximal engineering stress. Rather, the local microstructure in the crack location determines the maximum engineering stress in the tensile tests. Pores and other inhomogeneities introduce weak points, such that struts crack along these at lower stress.

The presented research provides a contribution in the understanding of the large variation in the mechanical properties of single *Al* foam struts. With that knowledge the manufacturing process can be improved. Less and smaller shrinking holes will lead to higher maximal technical stress until failure of the struts under tension. The variation in the mechanical properties will get smaller and the confidence in the mechanical properties get bigger, which will lead to a higher usage for larger applications.

5. Acknowledgments

The authors gratefully acknowledge the Daimler and Benz Foundation (project number 32-07/14) for financial support.

References

- [1] A. Jung, J. Luksch, S. Diebels, F. Schaefer, C. Motz, In-situ and ex-situ microtensile testing of individual struts of Al foamsand Ni/Al hybrid

- foams, *Mater. Des.* 153 (2018) 104–119 (2018).
- [2] J. Banhart, Manufacture, characterisation and application of cellular metals and metal foams, *Progress in materials science* 46 (6) (2001) 559–632 (2001).
 - [3] S. F. Fischer, Energy absorption efficiency of open-cell pure aluminum foams, *Materials Letters* 184 (2016) 208–210 (2016).
 - [4] F. García-Moreno, Commercial applications of metal foams: their properties and production, *Materials* 9 (2016) 85 (2016).
 - [5] D. K. Rajak, L. A. Kumaraswamidhas, S. Das, S. S. Kumaran, Characterization and analysis of compression load behaviour of aluminium alloy foam under the diverse strain rate, *Journal of Alloys and Compounds* 656 (2016) 218–225 (2016).
 - [6] T. A. Schaedler, W. B. Carter, Architected cellular materials, *Annual Review of Materials Research* 46 (2016) 187–210 (2016).
 - [7] M. Ashby, The mechanical properties of cellular solids, *Metallurgical Transactions A* 14 (9) (1983) 1755–1769 (1983).
 - [8] K. E. Evans, A. Alderson, Auxetic materials: Functional materials and structures from lateral thinking!, *Advanced Materials* 12 (2000) 617–628 (2000).
 - [9] H.-P. Degischer, B. Kriszt, *Handbook of Cellular Metals*, Wiley-VCH Weinheim, 2002 (2002).
 - [10] S. Nemat-Nasser, M. Hori, *Micromechanics: Overall Properties of Heterogeneous Materials*, Elsevier (1).
 - [11] M. Kader, M. Islam, M. Saadatfar, P. Hazell, A. Brown, S. Ahmed, J. Escobedo, Macro and micro collapse mechanisms of closed-cell aluminium foams during quasi-static compression, *Mater. Des.* 118 (2017) 11–21 (2017).
 - [12] A. Jung, Z. Chen, J. Schmauch, C. Motz, S. Diebels, Micromechanical characterisation of Ni/Al hybrid foams by nano- and microindentation coupled with EBSD, *Acta Materialia* 102 (2016) 38–48 (2016).

- [13] M. Mukherjee, F. García-Moreno, C. Jiménez, A. Rack, J. Banhart, Microporosity in aluminium foams, *Acta Materialia* 131 (2017) 156–168 (2017).
- [14] A. Jung, S. Diebels, Microstructural characterisation and experimental determination of a multiaxial yield surface for open-cell aluminium foams, *Materials & Design* 131 (2017) 252–264 (2017).
- [15] A. Jung, S. Diebels, Micromechanical characterization of metal foams, *Advanced Engineering Materials* 21 (2019).
- [16] M. A. Hasan, A. Kim, H.-J. Lee, Measuring the cell wall mechanical properties of Al-alloy foams using the nanoindentation method, *Composite Structures* 83 (2) (2008) 180–188 (2008).
- [17] C. Betts, D. Balint, J. Lee, J. Lin, P. Lee, In situ microtensile testing and X-ray microtomography-based finite element modelling of open-cell metal foamstruts and sandwich panels, *J Strain Analysis* 49 (2014) 592–606 (2014).
- [18] P. Schueler, F. Frank, D. Uebel, S. F. Fischer, A. Buuehrig-Polaczek, C. Fleck, Influence of heat treatments on the microstructure and mechanicalbehaviour of open cell AlSi7Mg0.3 foams on different length-scales, *Acta Materialia* 109 (2016) 32–45 (2016).
- [19] J. Weiler, J. Wood, R. Klassen, E. Maire, R. Berkmortel, G. Wang, Relationship between internal porosity and fracture strength of die-cast magnesium AM60B alloy, *Materials Science and Engineering A* 395 (2004) 315–322 (2004).
- [20] N. Vanderesse, E. Maire, A. Chabod, J.-Y. Buffiere, Microtomographic study and finite element analysis of the porosity harmfulness in a cast aluminium alloy, *International Journal of Fatigue* 33 (2011) 1514–1525 (2011).
- [21] S. F. Fischer, P. Schüler, C. Fleck, A. Bührig-Polaczeka, Influence of the casting and mould temperatures on the (micro)structure and compression behaviour of investment-cast open-pore aluminium foams, *Acta Materialia* 61 (2013) 5152–5161 (2013).

- [22] Y. Amani, S. Dancette, J. Luksch, A. Jung, E. Maire, Micro-tensile behavior of struts extracted from an aluminum foam, *Materials Characterization* 166 (2020) 110456 (2020).
- [23] J. Shouxun, W. Yang, F. Gao, D. Watson, Z. Fan, Effect of iron on the microstructure and mechanical property of Al–Mg–Si–Mn and Al–Mg–Si diecast alloys, *Mater. Sci. Eng., A* 564 (2013) 130–139 (2013).
- [24] J. A. Taylor, Iron-containing intermetallic phases in Al-Si based casting alloys, *Procedia Mater. Sci.* 1 (2012) 19–33 (2012).
- [25] L. Salvo, P. Cloetens, E. Maire, S. Zabler, J. J. Blandin, J. Y. Buffiere, W. Ludwig, E. Boller, D. Bellet, C. Josserond, X-ray micro-tomography an attractive characterisation technique in materials science, *Nucl. Instrum. Methods Phys. Res.* 200 (2003) 273–286 (2003).
- [26] E. Maire, P. J. Withers, Quantitative X-ray tomography, *International Materials Reviews* 59 (1) (2014) 1–43 (2014).
- [27] A. Jung, M. Wocker, Z. Chen, H. Seibert, Microtensile testing of open-cell metal foams - Experimental setup, micromechanical properties, *Materials & Design* 88 (2015) 1021–1030 (2015).
- [28] C. Schneider, W. Rasband, K. Eliceiri, Nih image to imagej: 25 years of image analysis, *Nature Methods* 9 (2012) 671–675 (2012).
- [29] Q. G. Wang, Microstructural effects on the tensile and fracture behavior of aluminum casting alloys A356/357, *Metallurgical and Materials Transactions A* 34 (2003) 2887–2899 (2003).
- [30] W. Jiang, Z. Fan, D. Liu, D. Liao, X. Dong, X. Zong, Correlation of microstructure with mechanical properties and fracture behavior of A356-T6 aluminum alloy fabricated by expendable pattern shell casting with vacuum and low-pressure, gravity casting and lost foam casting, *Materials Science and Engineering: A* 560 (2013) 396–403 (2013).